Progress in Physics of Applied Materials 6 (2026), Serial Number 10, 43 –55

Semnan University

Progress in Physics of Applied Materials

journal homepage: https://ppam.semnan.ac.ir/

Synthesis and Investigation of Different Properties of K_2FeO_4/ZnO and Its GO-Based Nanocomposites

Azam Hashemi[a], Mahmoud Naseri[a]*, Mohammad Mahdi Shahidi[b], Hossein Mojtabazadeh[c], Nasrin Salehi[d], Mahshid Chireh[a] *

[a]*Department of Physics, Faculty of Science, Malayer University, Malayer, Iran*
[b]*UNESCO-UNISA Africa Chair in Nanoscience and Nanotechnology College of Graduates Studies, University of South Africa, Muckleneuk Ridge, Pretoria, 392, South Africa*
[c]*Department of Organic Chemistry, Faculty of Chemistry, University of Kashan, Kashan, Iran*
[d]*Department of Basic Sciences, Shahrood Branch, Islamic Azad University, Shahrood, Iran*

ARTICLE INFO

Article history:
Received: 14 June 2025
Revised: 9 July 2025
Accepted: 10 July 2025
Published online: 3 September 2025

Keywords:
Nanoferrate;
Thermal treatment;
Dielectric;
Graphene oxide;
Photocatalytic.

ABSTRACT

This paper presents significant findings regarding the impact of ZnO and graphene oxide (GO) doping on the structural and electrical properties of potassium ferrate nanostructures. The samples were synthesized using a thermal treatment method at temperatures of 773, 873, and 973 K. The structural characteristics, optical and magnetic properties of the synthesized samples were analyzed using various techniques. The photocatalytic activity of K_2FeO_4/ZnO nanoparticles under visible light irradiation was investigated using methylene blue (MB) degradation as a probe reaction. The results indicated a significant enhancement in photocatalytic activity when GO was incorporated into the K_2FeO_4/ZnO nanocomposite. The dielectric constant and dielectric loss were measured at room temperature across a frequency range of 4 to 8 MHz using an LCR meter. Our findings reveal that the addition of graphene oxide (GO) did not result in a significant enhancement in dielectric permittivity compared to potassium ferrate/ZnO nanocomposites. Therefore, potassium ferrate-based nanocomposites, given their favorable dielectric properties, are promising candidates for a wide range of applications, including devices operating at microwave frequencies, various optical and microelectronic applications, and as materials for microwave absorption.

1. Introduction

The energy transition must address the dual challenge of meeting the demands of a growing, increasingly energy-intensive global economy while adhering to environmental and ecological constraints. In this context, there is a significant interest in the development of innovative environmental technologies for energy storage and recovery [1]. Composites have garnered considerable attention in recent years due to their potential to offer novel technological solutions with enhanced properties, particularly for advanced applications such as electronics, energy systems, and automotive technologies. For electrical applications specifically, the incorporation of metallic or ceramic micro/nanoparticles into a polymer matrix has been shown to confer desirable properties [2]. With the continued trend toward greater integration, miniaturization, and multifunctionality in modern electronics, nanocomposite materials with high dielectric permittivity are expected to see broader use in capacitors, field-effect transistors, memory devices, and energy storage systems [1]. Among energy storage devices, ceramic-based dielectric capacitors are particularly valued due to their high temperature stability, superior mechanical properties, and their ability to store large amounts of energy with fast charge-discharge rates [3]. However, the electronic industry still heavily relies on lead-based dielectric materials, which contribute to environmental pollution. Additionally, the non-stoichiometric composition of these dielectrics often requires high processing temperatures. Lead-free materials

* Corresponding author.
E-mail address: m.naseri@malayeru.ac.ir

Cite this article as:
Hashemi, A., Naseri, M., Shahidi, M.M., Mojtabazadeh, H., Salehi, N., and Chireh, M., 2026. Synthesis and Investigation of Different Properties of K_2FeO_4/ZnO and Its GO-Based Nanocomposites. *Progress in Physics of Applied Materials*, *6*(1), pp.43-55. DOI: 10.22075/ppam.2025.38094.1151

such as CuO, ZnO, and TiO_2, along with co-doping elements such as Fe, Na, Mg, Ag, Mn, and Al, have emerged as effective alternatives in this regard [4]. In fact, the chemical valence states of complex ions can be flexibly adjusted by regulating the ratio of co-doping ions. As the valence states of these complex ions change, it is expected that substitution types, relative concentrations of charge carriers, and the resulting dielectric behavior will also be altered. From the perspective of defect design, substituting complex ions with nonequivalent valence states can result in optimized dielectric properties, provided that overall charge balance is maintained [5]. The primary reason for introducing substitutional impurity ions is to increase the electrical resistivity of the composite, which is crucial for reducing electrical or dielectric losses, especially in high-frequency applications [6]. Among the various nanomaterials used in composite fabrication to enhance physical properties, graphene and graphene oxide (GO) are of particular importance due to their unique properties, such as exceptional stiffness, strength, high specific surface area, excellent thermal conductivity, and gas impermeability [7]. Graphene also exhibits high electron mobility and excellent electrical and chemical properties, which support the formation of nanoparticles in composite structures. Moreover, graphene's high dielectric properties contribute to low impedance and limited absorption characteristics, although its tendency to agglomerate can pose challenges [8]. In addition to their use in electronics and energy storage, nanocomposites, particularly those incorporating metal oxides like ZnO and graphene-based materials, are increasingly being investigated for their potential applications in various fields [9].

These materials can be employed in the development of smart fertilizers, which offer controlled release of nutrients and improve plant uptake efficiency. Zinc oxide (ZnO) nanoparticles, for instance, have been shown to enhance plant growth and yield by providing essential zinc nutrition more effectively than conventional fertilizers. Furthermore, graphene-based materials are being explored for their role in promoting seed germination, improving water retention in soil, and acting as carriers for agrochemicals, thereby reducing environmental pollution from excess chemical use [10]. Among the latest technologies, photocatalysis, an eco-friendly nanotechnology approach, offers a potentially sustainable solution to current agricultural environmental challenges. [11]. Therefore, researchers, have extensively investigated the photocatalytic degradation of water pollutants using various semiconductor oxide photocatalysts, including ZnO and TiO_2 [12, 13].

The simultaneous study of dielectric and photocatalytic properties in nanoparticles holds tremendous potential for advancing technologies in areas like water purification, solar energy conversion, and environmental remediation. Further investigation is crucial to unlock the full potential of these multifunctional nanomaterials. Accordingly, in this study, magnetic nanostructures of potassium ferrate -doped zinc oxide nanoparticles were synthesized using the thermal treatment method. In the next step, these nanoparticles were successfully anchored on graphene oxide sheets by hydrothermal method.

2. Experimental

2.1. Materials and Methodology

In the synthesis of K_2FeO_4/ZnO and K_2FeO_4/ZnO/GO deionized water as the solvent and metal nitrates as precursors and Polyvinylpyrrolidone (PVP) as the capping agent have been used. Iron nitrate, Fe $(NO_3)_3 \bullet 9H_2O$, and potassium nitrate, KNO_3, Zinc nitrate,$Zn(NO_3)_2$, were purchased from Acros Organics (99%). The following reagents, all obtained from Merck, were used as received without further purification: polyvinyl alcohol (PVA, MW = 31,000 g/mol), hydrogen peroxide (30% H_2O_2), graphite, ethanol, hydrochloric acid (37% HCl), potassium permanganate (99.5% $KMnO_4$), and sulfuric acid (98% H_2SO_4).

2.2. Synthesis of K_2FeO_4

The synthesis of potassium ferrate nanoparticles was achieved via a thermal treatment method. A solution of 4 g PVP in 100 mL of deionized water was prepared at 353 K. Subsequently, a solution containing 0.2 mmol potassium nitrate and 0.1 mmol iron nitrate (molar ratio K:Fe = 2:1) was added, and the mixture was stirred magnetically for 2 hours. Then, the mixture wasdried for 24 h at 353K in an oven. The calcination of the powder was performed at 723, 823, and 923K for 3h to crystallize nanocrystal and decompose organic material.

2.3. Synthesis of K_2FeO_4/ZnO

To synthesize K_2FeO_4/ZnO nanoparticles, again thermal treatment method was used. In this way that, 0.1 g of synthesized K_2FeO_4 nanoferrate was dispersed into 500 ml deionized water. The solution was placed in an ultrasonic unit for 30 min and then, 0.4 g of zinc nitrate and 19 g of PVP were slowly added to it and the mixture was dried 24 h at 353K in an oven. Finally, the powder was calcined at 723, 823, and 923K for 3h.

2.4. Synthesis of Graphene Oxide

Graphene oxide (GO) was synthesized via a modified Hummers method [14]. 1 g of graphite powder was added to a mixture of 3 g potassium permanganate ($KMnO_4$, 99.5% purity) and 25 mL concentrated sulfuric acid (H_2SO_4, 98% purity). This mixture was stirred for 3 hours at 20 °C. The resulting suspension was then diluted by slow addition of 100 mL deionized water and 5 mL of 30% hydrogen peroxide (H_2O_2). After 5 minutes of stirring, a bright yellow solution formed. This solution was centrifuged at 5000 rpm for 15 minutes, and the obtained solid was washed several times with 10% hydrochloric acid (HCl) and distilled water. The resulting yellow-brown precipitate was collected via filtration and dried under vacuum at 333 K for 24 hours.

2.5. Synthesis of K_2FeO_4/ZnO /GO

K_2FeO_4/ZnO/GO nanocomposites were prepared as follows: A dispersion of 2 g of GO in a 1:1 mixture of distilled water and ethanol (100 mL total volume) was prepared. Separately, 1.5 g of K_2FeO_4/ZnO nanopowder was dispersed in 100 mL of distilled water. The K_2FeO_4/ZnO dispersion was then slowly added to the GO

dispersion, and the resulting mixture was sonicated for 30 minutes. After sonication, the mixture was stirred for 24 hours. The resulting suspension was then centrifuged to separate the solid product, washed repeatedly with distilled water, and finally dried under vacuum at 60 °C for 24 hours to yield the K_2FeO_4/ZnO/GO nanocomposite.

3. Characterization Techniques

Morphological and structural properties of nanoferrate composites were investigated by X-ray diffraction (XRD, Panalytical X'Pert Pro-model from Netherlands, λ=1.54 Å), field emission-scanning electron microscopy (FESEM, Zeiss SIGMA VP from Germany) images TE-SCAN type instrument coupled with Energy dispersive X-ray spectroscopy (EDX) for elemental analysis, transmission electron microscopy (TEM, Zeiss EM10C; accelerating voltage 100 kV, Germany), and Fourier transform infrared (FT-IR, PerkinElmer Spectrum Two, USA) spectroscopy. The Digimizer image analysis software was used for calculating the average particle sizes. The band gap energies of the K_2FeO_4/ZnO and K_2FeO_4/ZnO/GO nanocomposites were analyzed by UV–visible absorption spectroscopy (UV1650PCSHIMADZU). The magnetic properties of all the synthesized samples were evaluated at room temperature via vibrating sample magnetometer (VSM) (VSM, DKB model), the magnetic characteristics were measured, and by using a laser Raman spectrophotometer (UniRAM, wavelength of excitation laser: 785 nm), Raman spectra were measured. Dielectric and impedance spectroscopy measurements were carried out in frequency range of 4Hz to 8 MHz using LCR meter (Model: HIOKI IM3536).

4. Results and Discussion

4.1. XRD Analysis

The crystal structure and phase composition of K_2FeO_4/ZnO and K_2FeO_4/ZnO/GO nanocomposites were examined using X-ray diffraction (XRD), as presented in Figure 1. In the XRD patterns of K_2FeO_4/ZnO nanocomposites, measured at three different temperatures (Figs. 1a, b, and c), peaks marked with squares correspond to the characteristic crystalline planes of K_2FeO_4, aligning with the orthorhombic structure (ICCD: 00-025-0652) [15]. Additional peaks observed in the XRD patterns correlate with the (100), (002), (101), (102), (110), (103), (200), and (112) crystallographic planes, confirming the presence of ZnO in the hexagonal wurtzite phase (JCPDS No. 36-1451) [16]. For the K_2FeO_4/ZnO/GO nanocomposite (Figs. 1d, e, and f), similar diffraction patterns were observed, suggesting the preservation of K_2FeO_4 and ZnO phases, while the absence of the GO peak indicates complete exfoliation of GO, likely due to the integration of K_2FeO_4/ZnO particles within the GO matrix [17]. The average crystallite sizes for both K_2FeO_4/ZnO and K_2FeO_4/ZnO/GO nanocomposites were calculated using the Scherrer equation $D=K\lambda/\beta\cos\theta$, where D represents the average crystallite size, K is the shape factor (0.9), λ is the wavelength of the X-ray radiation, β is the full width at half maximum (FWHM) of the peak, and θ is the diffraction angle [18]. The calculated crystallite sizes are presented in Table 1.

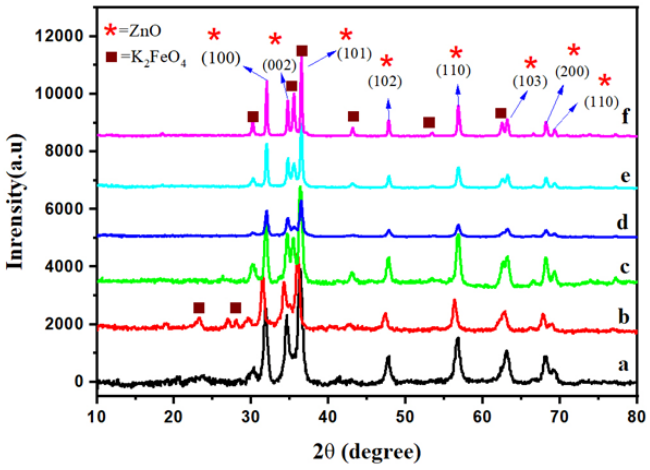

Fig. 1. XRD patterns of K_2FeO_4/ZnO calcined at (a) 723, (b) 823, and (c) 923 K, and K_2FeO_4/ZnO/GO calcined at (d) 723, (e) 823, and (f) 923 K.

4.2. FT-IR Analysis

Fourier-transform infrared (FTIR) spectroscopy was conducted to elucidate the structural properties, identify functional groups, and confirm the attachment of K_2FeO_4/ZnO nanoparticles onto GO sheets, as illustrated in Figure 2. Peaks observed at approximately 471 cm^{-1} and 544 cm^{-1} in Figure 2a, b, c, d, e, and f) correspond to characteristic vibrations of the Fe–O bond [19]. Additionally, metal-oxygen (M–O) bonds (where M represents Fe, K, or Zn) are indicated by peaks around 598 cm^{-1}, supporting the successful formation of the K_2FeO_4/ZnO nanocomposite [20]. Absorption bands within the 1400–2860 cm^{-1} range, found in all samples, likely indicate the presence of residual PVP surfactant from the synthesis process [21].

A strong band at 3340 cm^{-1} is attributed to O–H stretching, suggesting the presence of OH and/or COOH functional groups within the composite structure [22].

The peak at 1090 cm^{-1} corresponds to the ketone C–CO–C stretch within the aryl ether ring, while the phenol O–H bending appears at 1390 cm^{-1} [23].

Additionally, peaks at 1640 cm^{-1} and 1730 cm^{-1} are associated with the aromatic C=C skeletal vibration and C=O stretching, respectively [24].

Furthermore, although some absorption bands related to residual PVP and GO functional groups (e.g., C=O, C–O, and O–H) are still detectable, the appearance of distinct metal–oxygen bands (Fe–O around 471 and 544 cm^{-1}, and Zn–O near 598 cm^{-1}) clearly confirms the successful formation of the K_2FeO_4/ZnO composite structure and its effective anchoring onto the GO sheets.

These observations are consistent with previous reports and demonstrate the coexistence of precursor remnants and the final nanocomposite framework.

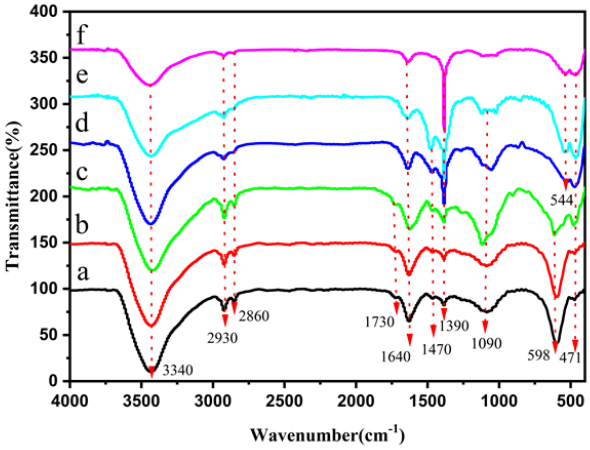

Fig. 2. FT-IR patterns of K_2FeO_4/ZnO calcined at (a) 723, (b) 823, and (c) 923 K, and K_2FeO_4/ZnO/GO calcined at (d) 723, (e) 823, and (f) 923 K.

4.3. FE-SEM, EDX, and TEM Analyses

The microstructure and morphology of K_2FeO_4/ZnO and K_2FeO_4/ZnO/GO nanocomposites were examined using field-emission scanning electron microscopy (FE-SEM) and transmission electron microscopy (TEM), as shown in Figures 3, 4, and 5. FE-SEM images (Fig. 3) reveal that K_2FeO_4/ZnO nanoparticles exhibit a spherical-like morphology with varying degrees of particle aggregation. To investigate the elemental composition of K_2FeO_4/ZnO and K_2FeO_4/ZnO/GO nanocomposites, EDX spectroscopy and EDS mapping were performed. Figure 4(a and b), provides insight into the spatial distribution and elemental composition of Zn, Fe, O, K, and C. The EDX spectrum of the K_2FeO_4/ZnO nanocomposite revealed the presence of Zn, Fe, K and O with weight percentages of 51.78%, 41.17%, 5.71%, and 1.34%, respectively (Fig. 4a). These results confirm that the nanocomposite is primarily composed of those four elements. Similarly, the EDX analysis of the K_2FeO_4/ZnO/GO nanocomposite showed the presence of Zn, Fe, K, and C with weight percentages of 44.97%, 8.96%, 25.08%, and 20.89%, respectively (Fig. 4b), confirming the successful incorporation of graphene oxide.

Table 1. Average particle sizes of K_2FeO_4/ZnO and K_2FeO_4/ZnO /GO calcined at different temperatures determined by XRD, and FESEM techniques.

Samples	**Average particle size XRD (nm)**	**Average particle size FESEM (nm)**
K_2FeO_4/ZnO (T=723 K)	19	28
K_2FeO_4/ZnO (T=823 K)	26	34
K_2FeO_4/ZnO (T=923 K)	32	41
K_2FeO_4/ZnO/GO (T=723 K)	17	25
K_2FeO_4/ZnO/GO (T=823 K)	22	29
K_2FeO_4/ZnO/GO (T=923 K)	27	35

In contrast, the K_2FeO_4/ZnO/GO nanocomposite displays small K_2FeO_4/ZnO particles distributed on and within the GO sheet surfaces, which is particularly evident in the TEM images (Fig. 5b). The TEM analysis of K_2FeO_4/ZnO (Fig. 5a) shows near-spherical nanoparticles with some agglomeration. This aggregation is likely due to strong interparticle interactions, including van der Waals forces and magnetic dipolar interactions, which can enhance the magnetic coupling within the nanocomposite [21].

4.4. UV-Vis Analysis

UV-Vis absorption spectra of the synthesized potassium ferrate nanocomposites doped with ZnO and GO were recorded over a wavelength range of 200–800 nm, as shown in Figure 6. The spectra display distinct absorption peaks attributed to electronic transitions within the material. For undoped potassium ferrate, the absorption edge lies in the UV region, with a sharp increase in absorbance below 400 nm, corresponding to the material's band gap absorption from the valence to the conduction band. Upon incorporation of ZnO and GO, a noticeable red-shift in the absorption edge occurs, indicating a reduction in band gap energy. This red-shift suggests successful integration of ZnO and GO within the potassium ferrate matrix, resulting in electronic structure modifications and enhanced light absorption in the visible region. The broader absorption bands in the visible spectrum further imply the formation of sub-bandgap states introduced by the dopants, which may improve the photocatalytic and optoelectronic properties of the material. The band gap energy (E_g) of the samples was calculated using the Tauc plot method, revealing a decrease in E_g with higher dopant concentrations. This reduction in band gap energy makes the nanocomposites suitable for applications in optoelectronics, visible-light photocatalysis, and energy storage devices. Changes in the energy gap can be better

understood if one considers that the interatomic spacing increases when the amplitude of the atomic vibrations increases due to the increased thermal energy [25]. On the other hand the observed red-shift in the absorption edge and the corresponding reduction in band gap energy with GO incorporation can be attributed to the electronic coupling and interfacial interactions between GO and the K_2FeO_4/ZnO nanostructure. GO, acting as an electron acceptor, introduces localized states within the band structure and promotes enhanced charge delocalization. Additionally, the increase in particle size at higher calcination temperatures (as confirmed by XRD and TEM data) contributes to band gap narrowing due to reduced quantum confinement. These effects collectively explain the observed trend in band gap reduction.

4.5. VSM Analysis

Vibrating Sample Magnetometry (VSM) was used to investigate the magnetic properties of K_2FeO_4/ZnO and K_2FeO_4/ZnO/GO nanocomposites calcined at 773, 873, and 973 K. The magnetization curves (M-H loops) provide insights into the magnetic behavior of these materials under an applied magnetic field.

Saturation Magnetization (M_s): The magnetization curves show varying saturation magnetization (M_s) values across the samples. For K_2FeO_4/ZnO, M_s values are 3.87, 3.75, and 2.93 emu/g for calcination temperatures of 773, 873, and 973 K, respectively. The K_2FeO_4/ZnO/GO samples show M_s values of 2.8, 2.76 and 1.65 emu/g for the same temperatures. The gradual decrease in M_s with increasing calcination temperature is attributed to temperature-induced microstructural changes. At higher calcination temperatures, although the overall crystallinity improves due to organic removal and grain growth, the formation of microstructural defects (e.g., oxygen vacancies or interfacial strains) may increase, which can locally affect magnetic ordering and reduce saturation magnetization. These subtle structural variations, although beneficial for charge transport and photocatalysis, can disrupt magnetic coherence and reduce the net magnetic response.

Comparison of Samples: K_2FeO_4/ZnO nanocomposites exhibit higher saturation magnetization compared to K_2FeO_4/ZnO/GO samples. This difference may stem from the presence of graphene oxide, which decreases the magnetic iron oxide content and introduces diamagnetic behavior, thereby diluting the overall magnetic response of the composite.

Magnetic Hysteresis: The narrow magnetic hysteresis loops observed indicate low coercivity and soft magnetic behavior in the nanocomposites, making them suitable for applications in magnetic memory devices and catalysis.

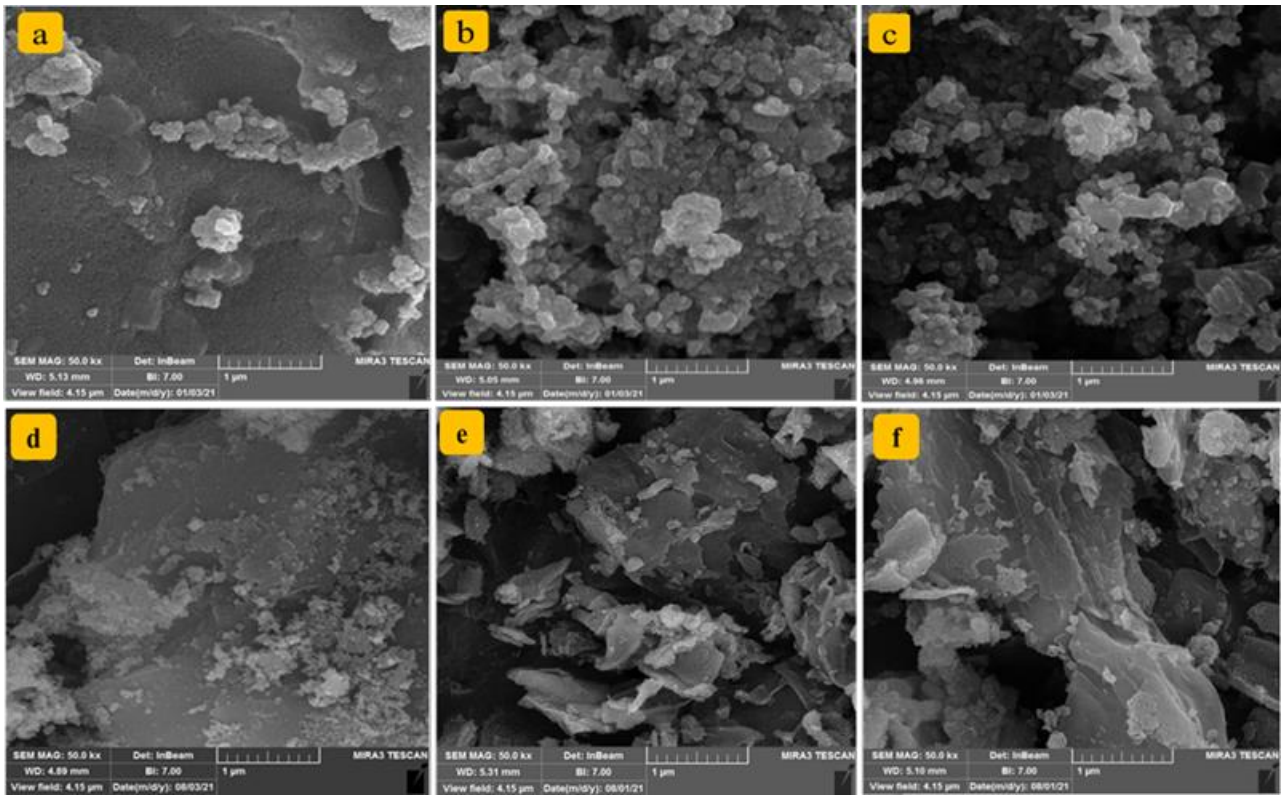

Fig. 3. FESEM images of K_2FeO_4/ZnO calcined at (a) 723, (b) 823, and (c) 923 K, and K_2FeO_4/ZnO/GO calcined at (d) 723, (e) 823, and (f) 923 K.

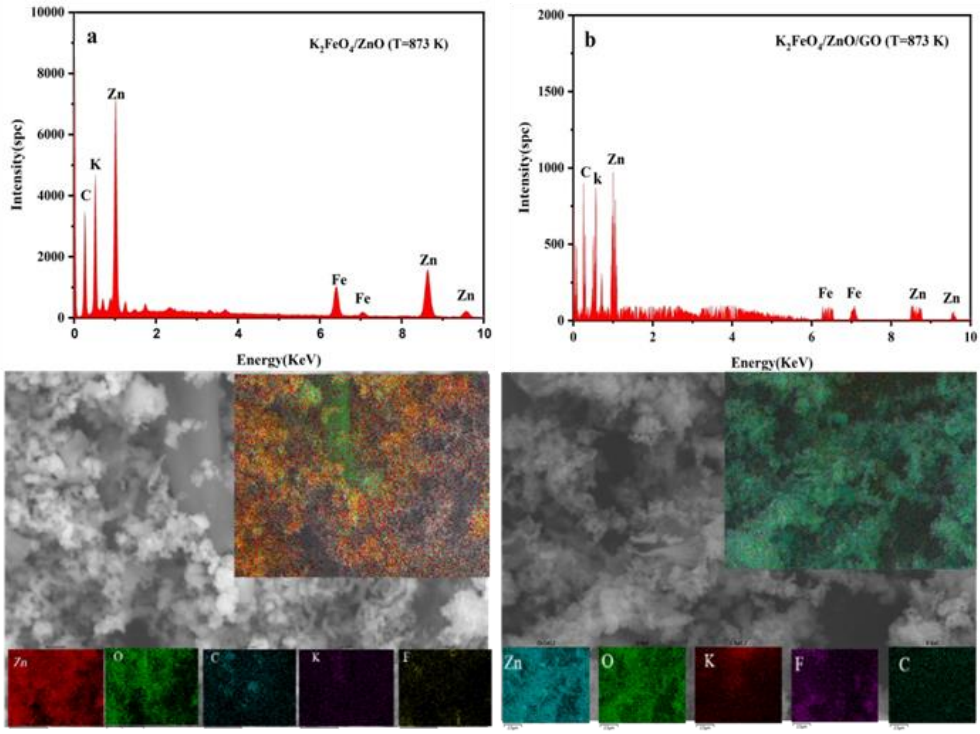

Fig. 4. EDX and map images of K_2FeO_4/ZnO ((a) T=823K), and K_2FeO_4/ZnO/GO ((b) T=823K).

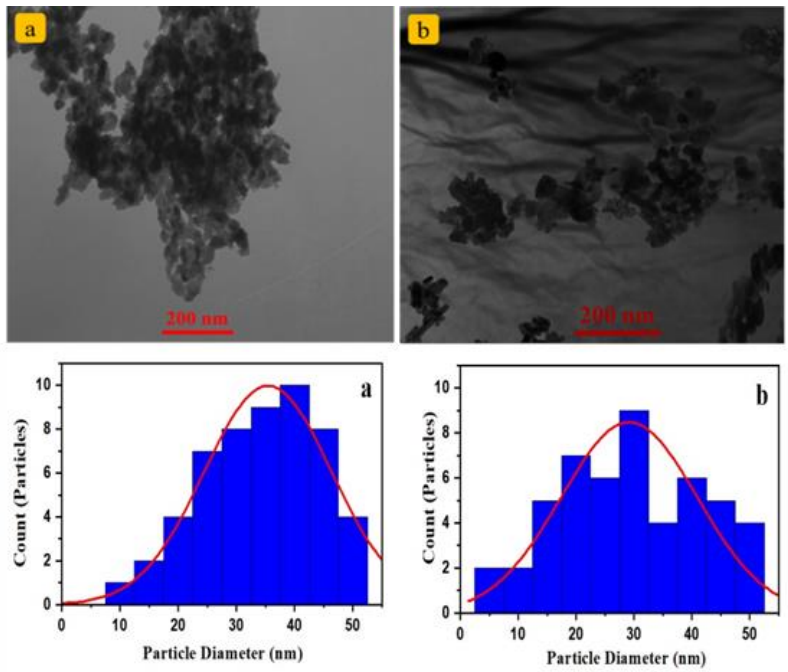

Fig. 5. TEM image and particle size distribution histograms (a) K_2FeO_4/ZnO calcined at 923 and (b) K_2FeO_4/ZnO/GO calcined at 923 K.

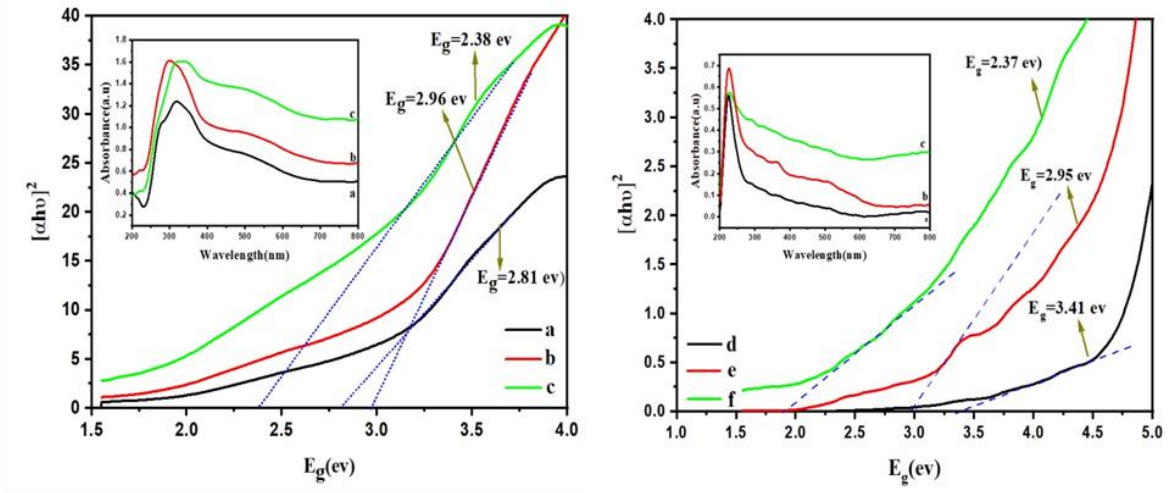

Fig. 6. UV patterns of K_2FeO_4/ZnO calcined at (a) 723, (b) 823, and (c) 923 K, and K_2FeO_4/ZnO/GO calcined at (d) 723, (e) 823, and (f) 923 K.

Effect of Temperature: As the calcination temperature increases, a decrease in saturation magnetization is observed, suggesting a decline in magnetic properties at higher temperatures. This effect may be attributed to reduced crystallite size and structural alterations induced by thermal treatment, which weaken magnetic interactions within the material [26]. VSM analysis reveals that both K_2FeO_4/ZnO and K_2FeO_4/ZnO/GO nanocomposites possess notable magnetic properties influenced by temperature and composition (Fig. 7). The higher saturation magnetization at lower calcination temperatures suggests these materials maintain superior magnetic properties when processed at lower temperatures. While the inclusion of GO reduces overall magnetization, it provides additional functionalities beneficial for applications such as magnetic storage and catalysis. A summary of magnetic parameters obtained from VSM spectra is provided in Table 2.

4.6. RAMAN Analysis

Raman spectroscopy was used to analyze the structural properties of K_2FeO_4/ZnO and K_2FeO_4/ZnO/GO nanocomposites calcined at temperatures of 773, 873, and 973 K, as shown in Figure 8. The spectra display characteristic peaks corresponding to ZnO, graphene oxide (GO), and iron oxide vibrational modes. Specifically, peaks at 370, 459, 644, and 840 cm^{-1} are associated with the A_1(TO), E_1(TO), and E_2(high) vibrational modes of ZnO [27]. The D and G bands of GO, prominent around 1352 and 1617 cm^{-1}, indicate the presence of sp^2-hybridized carbon atoms within the GO structure [28]. Additional peaks, such as the C–O stretch at 1448 cm^{-1} and CH_3 bending at 1774 cm^{-1}, further confirm the presence of functional groups and chemical bonding within the composite material. These observations suggest that the nanocomposites maintain a well-defined crystalline structure, with GO incorporation affecting the vibrational characteristics. This modification in vibrational properties contributes to the enhanced photocatalytic and electronic performance of the nanocomposites. The vibrational modes observed in the Raman spectra are in good agreement with the crystalline phases identified by XRD. Specifically, the strong Raman bands at 370, 459, and 644 cm^{-1} correspond to the ZnO E_2 and A_1(TO) modes, which confirm the hexagonal wurtzite structure also revealed by XRD. Furthermore, the presence of the D and G bands in the GO-containing samples (at ~1352 and ~1617 cm^{-1}, respectively) supports the effective incorporation of exfoliated graphene oxide, which was consistent with the disappearance of the GO peak in XRD patterns due to its exfoliated/disordered state. This trend is also observed in similar studies, such as [29], where the attenuation of the (002) XRD peak and preservation of Raman bands confirmed structural disruption and layer separation in graphite-based systems. Together, these findings reinforce the successful formation of a single-phase K_2FeO_4/ZnO/GO nanocomposite.

4.7. Dielectric Analysis

The dielectric properties of K_2FeO_4/ZnO and K_2FeO_4/ZnO/GO nanocomposites were examined using LCR (inductance, capacitance, resistance) analysis. The dielectric constant (ε′) and dielectric loss (tan δ) were measured across various frequencies and calcination temperatures (773 K, 873 K, and 973 K), as shown in Figures 9 and 10. For all samples, the dielectric constant decreases with increasing frequency, a typical behavior in dielectric materials that indicates interfacial polarization and dipole relaxation mechanisms within the composite. The incorporation of GO into the K_2FeO_4/ZnO matrix results in a higher dielectric constant at lower frequencies, likely due to increased interfacial polarization introduced by the GO layers. Additionally, dielectric loss decreases with frequency, suggesting reduced energy dissipation at higher frequencies. These trends indicate that the dielectric properties of the nanocomposites can be modulated by adjusting both the calcination temperature and GO content, making these materials promising for use in capacitors, sensors, and other electronic devices. Notably, the K_2FeO_4/ZnO/GO sample calcined at 973 K exhibited a distinctive dielectric loss profile compared to other samples. This anomaly is attributed to high-temperature-

induced structural rearrangements, possible partial reduction of GO, and enhanced interfacial polarization effects. These factors collectively may lead to increased conductive pathways and dipolar relaxation losses, as supported by similar observations in GO-based nanocomposites reported in the literature [29].

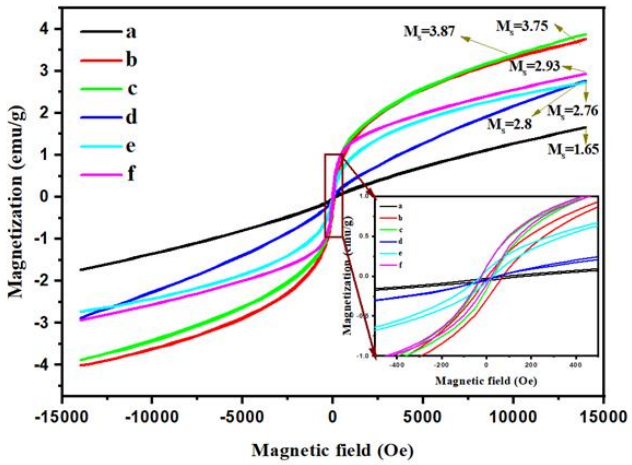

Fig. 7. VSM patterns of calcined at (a) 723, (b) 823, and (c) 923 K, and K_2FeO_4/ZnO/GO calcined at (d) 723, (e) 823, and (f) 923 K.

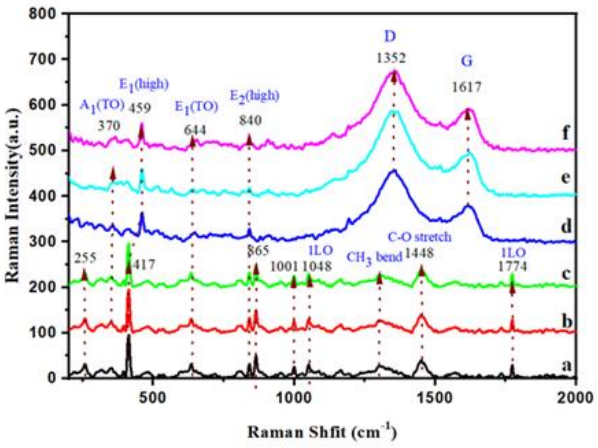

Fig. 8. RAMAN patterns of patterns of K_2FeO_4/ZnO calcined at (a) 723, (b) 823, and (c) 923 K, and K_2FeO_4/ZnO/GO calcined at (d) 723, (e) 823 and (f) 923 K.

4.8. Photocatalytic Analysis

The photocatalytic properties of K_2FeO_4/ZnO and K_2FeO_4/ZnO/GO nanocomposites were evaluated by assessing their ability to degrade Methylene Blue (MB) dye under visible light. Absorption spectra of the nanocomposites, calcined at 723, 823, and 923 K, were recorded in the wavelength range of 200–800 nm over a 90-minute irradiation period, with measurements taken at 15-minute intervals (Fig. 11). A reduction in the MB absorption peak intensity over time indicates effective photocatalytic degradation. Notably, samples calcined at 823 K and 923 K showed a more pronounced reduction in absorption, suggesting enhanced photocatalytic activity at higher calcination temperatures. The increase in photocatalytic properties of nanoparticles at high calcination temperatures is generally attributed to several interconnected factors such as improved crystallinity, increased particle size, reduced surface defects and removal of impurities [30] that improve their ability to absorb light and facilitate charge separation and transfer, leading to enhanced generation of reactive oxygen species (ROS). Calcination can increase particle size, thereby influencing the band gap and light absorption properties. In K_2FeO_4/ZnO nanoparticles, thermal calcination induces merging through grain boundary diffusion driven by zinc or oxygen defects [31]. the K_2FeO_4/ZnO/GO nanocomposite exhibited the most significant decline in absorbance, highlighting the synergistic effect of GO in enhancing light absorption and charge separation. The photocatalytic degradation efficiency (DE%) was calculated using the formula $DE(\%) = [(C_0 - C) / C_0] \times 100$, where C_0 is the initial concentration of MB, and C is the concentration after irradiation. Figure 12(a) illustrates the DE% of MB as a function of irradiation time for both nanocomposites. Results show that both K_2FeO_4/ZnO and K_2FeO_4/ZnO/GO nanocomposites exhibit photocatalytic activity, with K_2FeO_4/ZnO/GO achieving significantly higher degradation efficiency than K_2FeO_4/ZnO alone. After approximately 60 minutes, degradation rates stabilize, indicating that the photocatalytic process is nearing maximum efficiency. The DE% continues to increase with irradiation time, especially for K_2FeO_4/ZnO/GO, suggesting that GO enhances photocatalytic performance, particularly at higher calcination temperatures. In the context of first-order kinetic reactions, the expression $Ln(C_0/C)$ is used to describe the concentration changes of MB over time. Figure 12(b) shows that the composite containing GO has a greater increase in $Ln(C_0/C)$ over time than the composite without GO, confirming more efficient MB degradation in the presence of GO. At a calcination temperature of 923 K, this effect is particularly strong, likely due to improved crystallinity and surface properties of the nanocomposite, which further enhance photocatalytic performance. The combination of GO with K_2FeO_4/ZnO not only improves degradation efficiency but also accelerates reaction kinetics, underscoring the critical role of GO in optimizing the photocatalytic properties of the composite for environmental remediation applications. In summary, the improved photocatalytic activity of GO-based nanoparticles arises from a combination of enhanced light absorption, efficient charge separation and transport, increased surface area, and synergistic effects with other material [32]. GO acts as an electron acceptor, efficiently separating photogenerated electrons and holes. The electrons and the holes preventing recombination and improving the photocatalytic efficiency [33]. Table 3 provides a detailed breakdown of MB degradation percentages at 180 minutes of irradiation for each calcination temperature (723, 823, and 923 K), indicating that higher calcination temperatures yield greater MB degradation and enhanced photocatalytic performance.

Table 2. Magnetic parameters obtained from VSM spectrum.

Samples	M_s (emu/g)	M_r(emu/g)	(M_r/M_s)	H_C (Oe)
K_2FeO_4/ZnO (T=723 K)	1.65	~0	~0	~74
K_2FeO_4/ZnO (T=823 K)	3.75	~0/05	0/01	~70
K_2FeO_4ZnO (T=923 K)	3.87	~0/13	0/03	~27
K_2FeO_4/ZnO/GO (T=723 K)	2.18	~0/02	0/009	~50
K_2FeO_4/ZnO/GO (T=823 K)	2.76	~·/07	0/02	~25
K_2FeO_4/ZnO/GO (T=923 K)	2.93	~·/12	0/04	~14

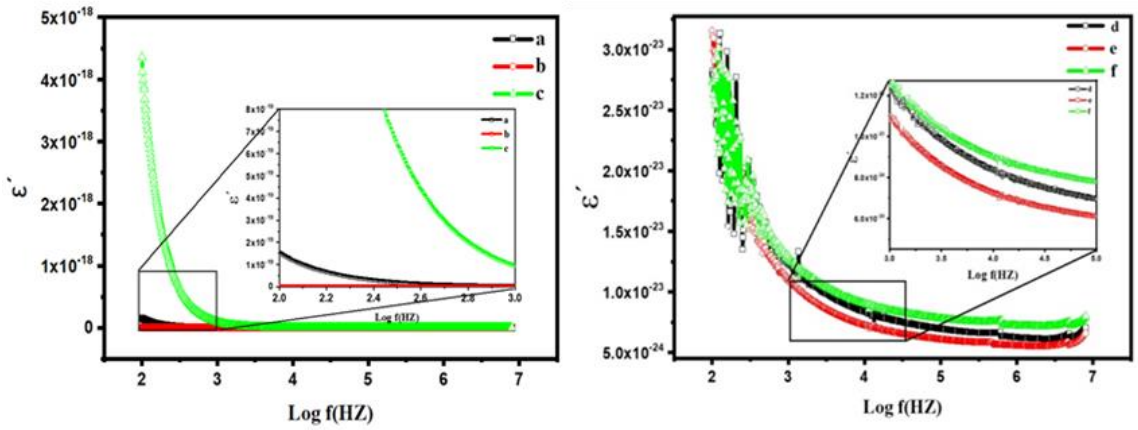

Fig. 9. Relationship between: dielectric constant and frequency of K_2FeO_4/ZnO calcined at (a) 723, (b) 823, and (c) 923 K, and K_2FeO_4/ZnO/GO calcined at (d) 723, (e) 823, and (f) 923 K.

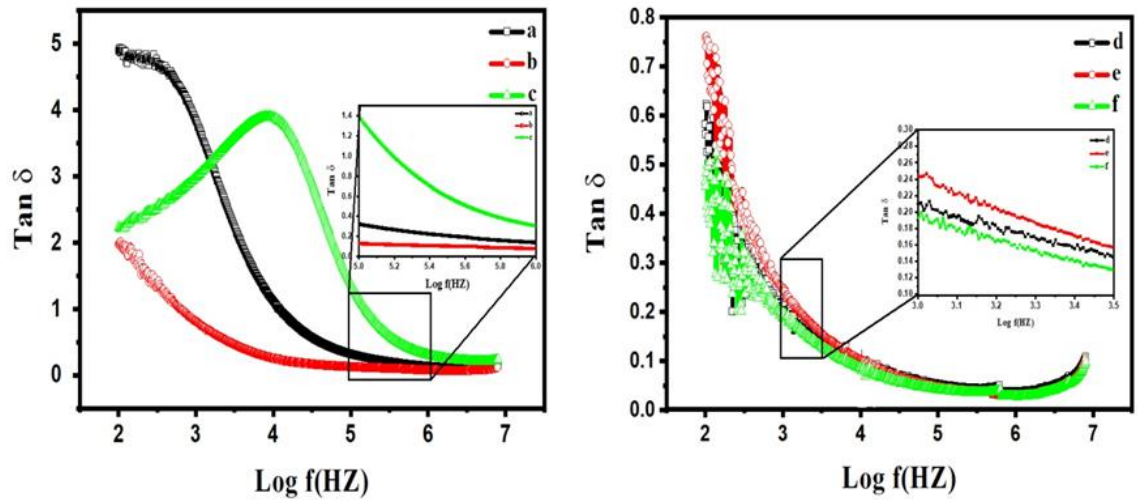

Fig. 10. Relationship between: dielectric loss tangent and frequency of patterns of K_2FeO_4/ZnO calcined at (a) 723, (b) 823, and (c) 923 K, and K_2FeO_4/ZnO/GO calcined at (d) 723, (e) 823, and (f) 923 K.

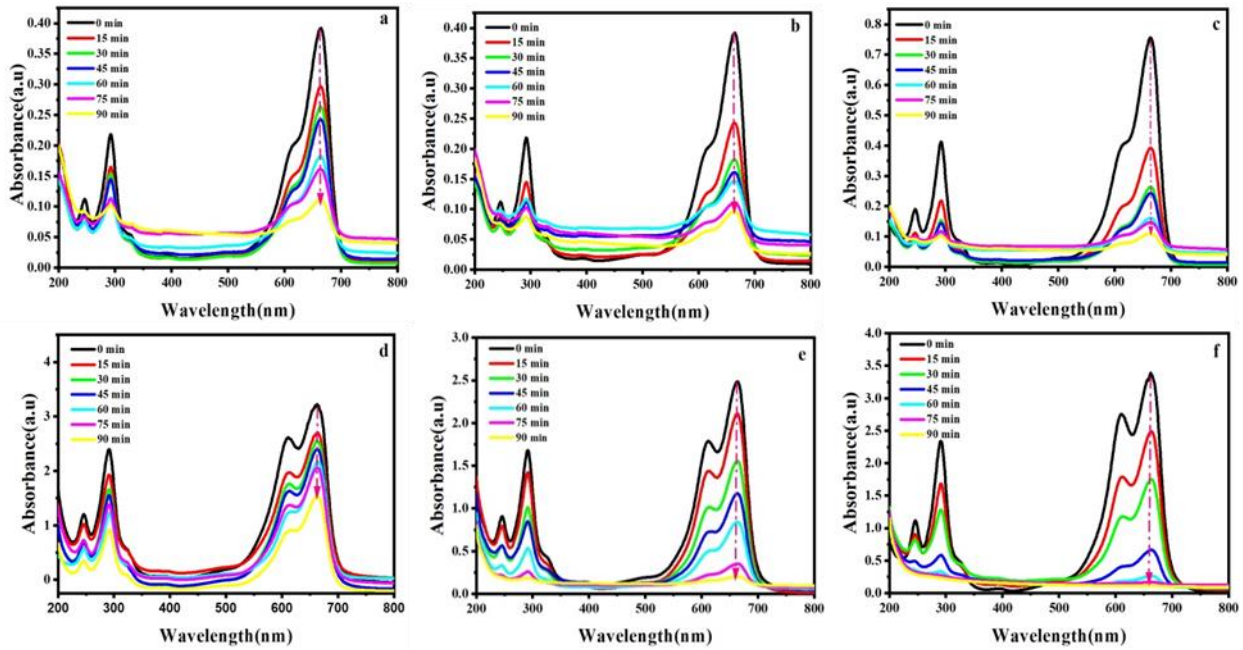

Fig. 11. Absorption spectra of the MB solution taken at different photocatalytic degradation times using of K_2FeO_4/ZnO calcined at (a) 723, (b) 823, and (c) 923 K, and K_2FeO_4/ZnO/GO calcined at (d) 723, (e) 823, and (f) 923 K.

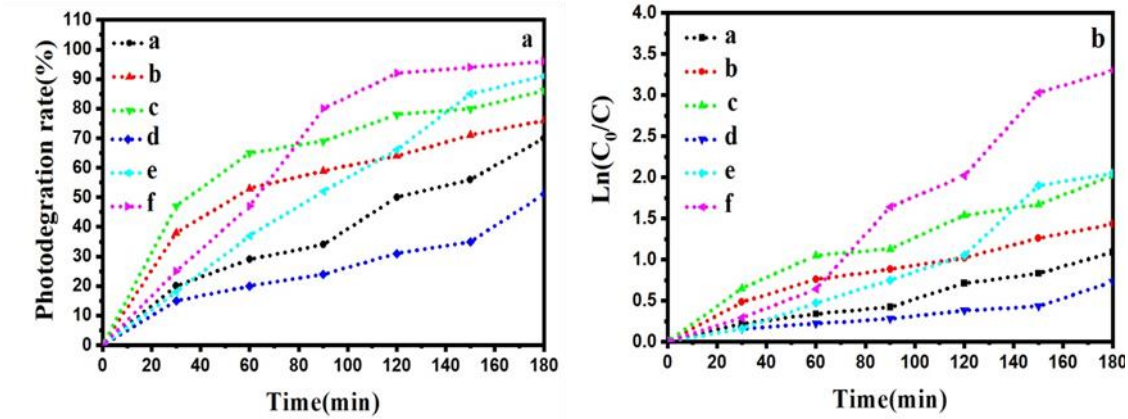

Fig. 12. (A) photocatalytic percent degradation of MB of K_2FeO_4/ZnO calcined at (a) 723, (b) 823, and (c) 923 K, and K_2FeO_4/ZnO/GO calcined at (d) 723, (e) 823 and (f) 923 K, and (B) Photodegradation rate of MB in solution of K_2FeO_4/ZnO calcined at (a) 723, (b) 823, and (c) 923 K, and K_2FeO_4/ZnO/GO calcined at (d) 723, (e) 823, and (f) 923 K.

Table 3. The photocatalytic degradation efficiency and the pseudo first order rate constant values for the of K_2FeO_4/ZnO and K_2FeO_4/ZnO/GO nanocomposites.

Samples	Calcination Temp. (K)	Irradiation time (min)	Photodegration rate (%)	Ln(C/C_0)
K_2FeO_4/ZnO	T=723	180	70	1.09
K_2FeO_4/ZnO	T=823	180	75	1.46
K_2FeO_4/ZnO	T=923	180	86	2.02
K_2FeO_4/ZnO/GO	T=723	180	51	0.73
K_2FeO_4/ZnO/GO	T=823	180	91	2. 5
K_2FeO_4/ZnO/GO	T=923	180	96	3.4

4.9. General Remarks and Future Outlook

This study highlights the multifunctional behavior of K_2FeO_4/ZnO/GO nanocomposites, where the incorporation of GO markedly enhanced photocatalytic activity under visible light due to improved charge separation, interfacial contact, and light absorption.

The highest degradation efficiency of methylene blue was achieved at 923 K, while soft magnetic behavior at lower temperatures supports potential applications in magneto-photocatalytic systems. However, the limited impact of GO on dielectric permittivity suggests the need for further interfacial engineering or incorporation of additional dielectric-active phases**.** To expand the

functionality and efficiency of these composites, several future directions are proposed:

Layered architecture optimization: Inspired by $SnO_2/Ag/SnO_2$ multilayers, designing $K_2FeO_4/ZnO/GO$ films with graded or multilayered structures may improve visible light transmission, infrared reflectance, and reduce sheet resistance, enabling applications in thermal insulation and optoelectronics [34].

Biopolymer-based dispersion enhancement: Glucosamine and chitosan, due to their abundant hydroxyl and amine groups, offer strong coordination with metal oxide surfaces and can prevent nanoparticle aggregation [35]. Glucosamine, a naturally occurring amino sugar, is widely used in pharmaceutical and biomaterial applications due to its biocompatibility and bioactivity [36]. These properties, combined with its functional amine and hydroxyl groups, suggest it could serve as a green modifier or bio-linker in photocatalytic and dielectric nanocomposites. Glucosamine has been shown to control particle dispersion and enhance surface area and photocatalytic activity in TiO_2/graphene composites [37]. Such strategies could be extended to $K_2FeO_4/ZnO/GO$ systems for improving catalytic and dielectric behavior.

Antimicrobial-functional hybrid materials: Inspired by $AgFe_2O_4/SiO_2$/Passiflora-based nanocomposites, which exhibited superior antimicrobial activity [38], $K_2FeO_4/ZnO/GO$ composites could be modified with Ag^+ ions, ferrite phases, or biocompatible agents to achieve dual photocatalytic–antibacterial functionality, ideal for water purification or biomedical coatings.

Multifunctional catalytic platforms: $Cu_2V_2O_7$ nanoparticles have shown efficient photocatalytic and organic synthetic activity, including recyclability in heterocyclic synthesis [39]. Incorporating such vanadates into the $K_2FeO_4/ZnO/GO$ framework may expand its role beyond pollutant degradation to broader green chemical transformations.

Perovskite-based enhancement: $CeFeO_3$/GO nanocomposites exhibited 97% MB degradation in just 25 minutes under visible light, attributed to strong GO-$CeFeO_3$ interaction and reduced crystallite size [40]. This suggests the potential of Ce- or La-based perovskites as additional components in future designs of $K_2FeO_4/ZnO/GO$ nanohybrids for advanced visible-light photocatalysis.

Overall, this research establishes a foundation for tailoring K_2FeO_4-based systems toward high-performance, multifunctional materials applicable in energy conversion, environmental remediation, catalysis, and potentially biomedical technologies.

5. Conclusions

This paper presents significant findings regarding the impact of ZnO and GO doping on the structural and electrical properties of potassium ferrate nanostructures. The samples were synthesized using a thermal treatment method at temperatures of 723, 823, and 923 K. The structural characteristics of the synthesized samples were analyzed using various techniques, including X-ray diffraction (XRD), field emission scanning electron microscopy (FESEM), energy-dispersive X-ray spectroscopy (EDS), transmission electron microscopy (TEM), ultraviolet-visible (UV-Vis) spectroscopy, vibrating sample magnetometry (VSM), Raman spectroscopy, and Fourier transform infrared (FTIR) spectroscopy. XRD and TEM analyses confirmed the formation of all samples with minimal impurities, and the average crystallite size was observed to range between 30 nm and 40 nm. The dielectric constant and dielectric loss were measured at room temperature across a frequency range of 4 Hz to 8 MHz using an LCR meter. Our findings reveal that the addition of graphene oxide (GO) did not result in a significant enhancement in dielectric permittivity compared to potassium ferrate/ZnO nanocomposites. Therefore, potassium ferrate-based nanocomposites, given their favorable dielectric properties, are promising candidates for a wide range of applications, including devices operating at microwave frequencies, various optical and microelectronic applications, and as materials for microwave absorption. The synthesized K_2FeO_4/ZnO nanocomposites with GO sheets demonstrated superior photocatalytic activity compared to pure K_2FeO_4/ZnO nanoparticles, as evidenced by their more efficient degradation of MB dye under visible light irradiation.

Funding Statement

This work was supported by the Ministry of Science Research and Technology of Iran under the FRGS grant, Malayer University of Iran.

Conflicts of Interest

The authors declare that they have no known competing financial interests or personal relationships that could have appeared to influence the work reported in this paper.

Authors Contribution Statement

Conceptualization and study design: Azam Hashemi, Mahmoud Naseri, Mohammad Mahdi Shahidi
Data collection and experimentation: Azam Hashemi, Mahmoud Naseri, Mohammad Mahdi Shahidi
Hossein Mojtabazadeh, Nasrin Salehi, Mahshid Chireh
Data analysis and interpretation: Azam Hashemi, Mahmoud Naseri, Mohammad Mahdi Shahidi
Hossein Mojtabazadeh, Nasrin Salehi, Mahshid Chireh
Manuscript writing and editing: Azam Hashemi, Mahmoud Naseri
Supervision and project administration: Mahmoud Naseri

References

[1] Zahid, M., Touili, S., Mezzane, D., Gouné, M., Uršič, H., Šadl, M., Elamraoui,Y., Hoummada,Kh.,Kutnjak,Z. and El Marssi, M. 2023. Dielectric and energy storage properties of surface-modified $BaTi_{0.89}Sn_{0.11}O_3$@ polydopamine nanoparticles embedded in a PVDF-HFP matrix. *RSC advances, 13*(37), pp.26041-26049.

[2] Ciobanu, R. C., Damian, R. F., Schreiner, C. M., Aradoaei, M., Sover, A. and Raichur, A. M. 2023. Simulation of Dielectric Properties of Nanocomposites with Non-Uniform Filler Distribution. *Polymers, 15*(7), p.1636.

[3] Qiao, X., Zhang, X., Wu, D., Chao, X. and Yang, Z. 2018. Influence of Bi nonstoichiometry on the energy storage properties of 0.93KNN–0.07Bi_xMN relaxor ferroelectrics. Journal of *Advanced Dielectrics, 8*(06), p.1830006.

[4] Shaheen, K., Shah, Z., Arshad, T., Ma, L., Liu, M., Wang, Y., Cui., J. and Suo, H. 2020. Electrical, dielectric and photocatalytic applications of iron-based nanocomposites. *Applied Physics A, 126*, pp.1-10.

[5] Pan, W., Cao, M., Hao, H., Yao, Z., Yu, Z. and Liu, H. 2020. Defect engineering toward the structures and dielectric behaviors of (Nb, Zn) co-doped $SrTiO_3$ ceramics. *Journal of the European Ceramic Society, 40*(1), pp.49-55.

[6] Wahba, A. M., and Mohamed, M. B. 2014. Structural, magnetic, and dielectric properties of nanocrystalline Cr-substituted Co0. 8Ni0. $2Fe_2O_4$ ferrite. *Ceramics International, 40*(4), pp.6127-6135.

[7] Sadasivuni, K. K., Ponnamma, D., Kumar, B., Strankowski, M., Cardinaels, R., Moldenaers, P., Thoms., S. and Grohens, Y. 2014. Dielectric properties of modified graphene oxide filled polyurethane nanocomposites and its correlation with rheology. *Composites Science and Technology, 104*, pp.18-25.

[8] Mehmood, K., Rehman, A. U., Amin, N., Morley, N. A. and Arshad, M. I. 2023. Graphene nanoplatelets/Ni-Co-Nd spinel ferrite composites with improving dielectric properties. *Journal of Alloys and Compounds, 930*, pp.167335.

[9] Chireh, M., Naseri, M., Rahimi, M., Soleymani, A. R., 2024. Synthesis ZnO/RGO nanocomposite: Structural characteristics and antifungal/antibacterial properties. *Progress in Physics of Applied Materials, 4*, pp.77-81.

[10] Prasad, R., Bhattacharyya, A. and Nguyen, Q. D. 2017. Nanotechnology in Sustainable Agriculture: Recent Developments, Challenges, and Perspectives. *Frontiers in Microbiology, 8*, p.1014.

[11] Rodríguez-González, V., Terashima, C., and Fujishima, A. 2019. Applications of photocatalytic titanium dioxide-based nanomaterials in sustainable agriculture. *Journal of Photochemistry and Photobiology C: Photochemistry Reviews*, *40*, pp.49-67.

[12] Amiri, H., Nabizadeh, R., Martinez, S. S., Shahtaheri, S. J., Yaghmaeian, K., Badiei, A., and Naddafi, K., 2018. Response surface methodology modeling to improve degradation of Chlorpyrifos in agriculture runoff using TiO_2 solar photocatalytic in a raceway pond reactor. *Ecotoxicology and environmental safety, 147,* pp.919-925.

[13] El-Saeid, M. H., BaQais, A., & Alshabanat, M., 2022. Study of the photocatalytic degradation of highly abundant pesticides in agricultural soils. *Molecules*, *27*(3), p.634.

[14] Anajafi, Z., Naseri, M., Hashemi, A. and Neri, G., 2023. Structural and photocatalytic properties of $CeFeO_3$ and $CeFeO_3$/GO nanostructures. *Journal of Sol-Gel Science and Technology, 105*(1), pp.116-126.

[15] Hashemi, A., Naseri, M. and Chireh, M. 2021. Evaluation of physical properties, mechanism and photocatalytic activities of potassium ferrate nanostructures as an adsorbent for MB dye under UV light. *Applied Physics A, 127*(10), p.743.

[16] Chireh, M., Karam, Z. M., Naseri, M., Jafarinejad-Farsangi, S. and Ghaedamini, H. 2022. Synthesis, characterization and cytotoxicity study of graphene/doped ZnO/SiO_2 nanocomposites. *Applied PhysicsA, 128*(4), p.307.

[17] Omar, F. S., Nay Ming, H., Hafiz, S. M. and Ngee, L. H. 2014. Microwave synthesis of zinc oxide/reduced graphene oxide hybrid for adsorption-photocatalysis application. *International Journal of Photoenergy, 2014*(1), p.176835.

[18] Chireh, M., Naseri, M., and Kamalianfar, A. 2020. 57Fe Mossbauer spectroscopy investigation of $NiFe_2O_4$ and $MnFe_2O_4$ ferrite nanoparticles prepared by thermal treatment method. *Applied Physics A*, 126(7), p.543.

[19] Zulfiqar Ahmed, M. N., Chandrasekhar, K. B., Jahagirdar, A. A., Nagabhushana, H. and Nagabhushana, B. M. 2015. Photocatalytic activity of nanocrystalline ZnO, α-Fe_2O_3 and $ZnFe_2O_4$/ZnO. *Applied Nanoscience, 5*, pp.961-968.

[20] Zamani, M., Naderi, E., Aghajanzadeh, M., Naseri, M., Sharafi, A. and Danafar, H. 2019. $Co_{1-x}Zn_xFe_2O_4$ based nanocarriers for dual-targeted anticancer drug delivery: Synthesis, characterization and in vivo and in vitro biocompatibility study. *Journal of molecular liquids, 274*, pp.60-67.

[21] Chireh, M., Naseri, M., &Ghaedamini, H. 2021. Enhanced microwave absorption performance of graphene/doped Li ferrite nanocomposites. *Advanced Powder Technology, 32*(12), pp.4697-4710.

[22] Salimi, N., Mohammadi-Manesh, E., Ahmadvand, N., Danafar, H. and Ghiasvand, S. 2024. Curcumin-Loaded by Fe_3O_4/GO and Fe_3O_4/ZnO/GO Nanocomposites for Drug Delivery Applications: Synthesis, Characterization and Anticancer Assessment. *Journal of Inorganic and Organometallic Polymers and Materials, 34*(3), pp.1256-1271.

[23] Safari, M., Naseri, M., Naderi, E. and Esmaeili, E. 2022. Magnetically targeted delivery of Quercetin-loaded Ca1–x Mn x Fe_2O_4nanocarriers: synthesis, characterization and in vitro study on HEK 293-T and MCF-7 cell lines. *Applied Physics A, 128*(6), p.486.

[24] Liu, P., Yao, Z. and Zhou, J. 2015. Preparation of reduced graphene oxide/Ni0. 4Zn0. 4Co0. $2Fe_2O_4$ nanocomposites and their excellent microwave absorption properties. *Ceramics International, 41*(10), pp.13409-13416.

[25] Naseri, M., 2015. Optical and magnetic properties of monophasic cadmium ferrite ($CdFe_2O_4$) nanostructure prepared by thermal treatment method. *Journal of Magnetism and Magnetic Materials,* 392, 107-113.

[26] Safari, M., Naseri, M., Esmaeili, E., and Naderi, E. 2023. Green synthesis by celery seed extract and improvement of the anticancer activity of quercetin-loaded rGO/Ca1-xMnxFe_2O_4 nanocarriers using UV light in breast cancer cells. *Molecular Structure, 1281*, p.135059.

[27] Mathai, J., Jose, A. K., Anjana, M. P., Aleena, P. A., Kunjumon, J., Ittyachan, R. and Sajan, D. 2023. Substantial effect of Cr doping on the third-order nonlinear optical properties of ZnO nanostructures. *Optical Materials, 142*, p.114128.

[28] Chireh, M., Naseri, M., andGhiasvand, S. 2019.Enhanced photocatalytic and antibacterial activities of RGO/$LiFe_5O_8$ nanocomposites. *Journal of Photochemistry and Photobiology A: Chemistry, 385*, p.112063.

[29] Mojtabazadeh, H., & Safaei-Ghomi, J. 2025. High conductivity graphite paste for radio frequency identification tag with wireless hydrogen sensor based on CeO_2–Fe_2O_3–graphene oxide. *RSC Advances*, *15*(16), pp.12773–12784.

[30] Phromma, S., Wutikhun, T., Kasamechonchung, P., Eksangsri, T., and Sapcharoenkun, C. 2020. Effect of

calcination temperature on photocatalytic activity of synthesized TiO_2 nanoparticles via wet ball milling sol-gel method. *Applied sciences*, *10*(3), p.993.

[31] Li, D., Song, H., Meng, X., Shen, T., Sun, J., Han, W., and Wang, X. 2020. Effects of particle size on the structure and photocatalytic performance by alkali-treated TiO_2. *Nanomaterials, 10*(3), p.546.

[32] Tewari, C., Tatrari, G., Kumar, S., Pathak, M., Rawat, K. S., Kim, Y. N., and Sahoo, N. G. 2023. Can graphene-based composites and membranes solve current water purification challenges-a comprehensive review. *Desalination, 567*, p.116952.

[33] Ahmad, H., Fan, M., and Hui, D. 2018. Graphene oxide incorporated functional materials: A review. *Composites Part B: Engineering, 145*, pp.270-280.

[34] Shahriari, E., Raeisi, M., & Alamdari, S. 2025. Simulation and Fabrication of Three-Layer SnO_2/Ag/SnO_2 Nanostructure Coating for Energy Storage. *Progress in Physics of Applied Materials*, *5*(1), pp.17-22.

[35] Mousavi-Ebadi, M., Safaei-Ghomi, J., & Mojtabazadeh, H. 2025. Anchoring cobalt nanoparticles on to the grafted mono(6-ethylene-diamino-6-deoxy)-β-cyclodextrin to magnetic chitosan for enhanced catalytic performance of the synthesis of pyrano[2,3-c]pyrazole-3-carboxylates. *Carbohydrate Polymer Technologies and Applications*, pp.100923.

[36] Mojtabazadeh, H., & Safaei-Ghomi, J. 2025. Sustainable electrochemical depolymerization of chitosan into glucosamine hydrochloride using N-hydroxyphthalimide as a redox catalyst. *Carbohydrate Polymers*, pp.124008.

[37] Gu, L., Zhang, H., Jiao, Z., Li, M., Wu, M., & Lei, Y. 2016. Glucosamine-induced growth of highly distributed TiO_2 nanoparticles on graphene nanosheets as high-performance photocatalysts. *RSC advances*, *6*(71), pp.67039–67048.

[38] Hashemi, A., Tavafi, H., Naseri, M., Mojtabazadeh, H., Abedi, M., & Tork, N. 2024. Structural and antibacterial properties of $AgFe_2O_4$ and Fe_3O_4 nanoparticles, and their nanocomposites. *Progress in Physics of Applied Materials*, *4*(1), pp.37–46.

[39] kafi ahmadi, L., & khademinia, s. 2022. Fabrication of 3,4-dihydropyrimidin-2-(1H)-ones/thione compounds via $Cu_2V_2O_7$ nanocatalyst synthesized by solid state method. *Progress in Physics of Applied Materials*, *2*(1), pp.49-56.

[40] Anajafi, Z., Naseri, M., Hashemi, A., & Neri, G. 2023. Structural and photocatalytic properties of $CeFeO_3$ and $CeFeO_3$/GO nanostructures. *Journal of Sol-Gel Science and Technology*, *105*(1), pp.116–126.